Radiation Modeling for the Reentry of the Hayabusa Sample Return Capsule

Michael W. Winter*
University of Kentucky, Lexington, KY 40506-0503

Ryan D. McDaniel†, Yih-Kanq Chen‡
NASA Ames Research Center, Moffett Field, CA 94035

David Saunders§
ERC, Incorporated, NASA Ames Research Center, Moffett Field, CA 94035

and
Peter Jenniskens**
SETI Institute, 189 Bernardo Avenue, Mountain View, CA 94043

Predicted shock-layer emission signatures during the reentry of the Japanese Hayabusa capsule are presented and compared with flight measurements conducted during an airborne observation mission in NASA's DC-8 Airborne Laboratory. For selected altitudes at 11 points along the flight trajectory of the capsule, lines of sight were extracted from flow field solutions computed using the in-house high-fidelity CFD code, *DPLR*. These lines of sight were used as inputs for the line-by-line radiation code *NEQAIR*, and emission spectra of the air plasma were computed in the wavelength range from 300 nm to 1600 nm, a range which covers all of the different experiments onboard the DC-8. In addition, the computed flow field solutions were post-processed with the material thermal response code *FIAT*, and the resulting surface temperatures of the heat shield were used to generate thermal emission

* Research Scientist, Optical Plasma Diagnostics, University Affiliated Research Center UARC, University of California in Santa Cruz, CA, Current: Assistant Professor, Department of Mechanical Engineering, 287 Ralph G. Anderson Building, Lexington, KY 40506-0503, USA, Michael.Winter@uky.edu , Associate Fellow AIAA.
† Research Scientist, Aerothermodynamics Branch, NASA Ames Research Center, Ryan.D.McDaniel@nasa.gov, AIAA Member
‡ Aerospace Engineer, Aerothermodynamics Branch, , NASA Ames Research Center, Y-K.Chen@nasa.gov, AIAA Member
§ Senior Research Scientist, ERC, Inc. at NASA Ames Research Center. Current: Senior Research Scientist with AMA, Inc., David.Saunders@nasa.gov, AIAA Senior Member
** Hayabusa Observation Mission Principal Investigator, Carl Sagan Center, 515 North Whisman Road, Mountain View, CA 94043. Petrus.M.Jenniskens@nasa.gov, AIAA Member.

spectra based on Planck radiation. Both spectra were summed and integrated over the flow field. The resulting emission at each trajectory point was propagated to the DC-8 position and transformed into incident irradiance to be finally compared with experimental data.

Nomenclature

2D	two-dimensional
3D	three-dimensional
α	half opening angle
AUS	Australian Ultraviolet Spectrometer, observation set up, University of Queensland
a_w	speed of sound at the wall
c	speed of light in vacuum, 299,792,458 m/s
C	atomic carbon
C_2	molecular carbon
CEV	Crew Exploration Vehicle
CO	carbon oxide
CN	carbon nitride
CFD	computational fluid dynamics
DC-8	NASA's flying observatory
DPLR	Data-Parallel Line Relaxation algorithm, computational fluid dynamics code
e-	electrons
$\Delta\lambda$	wavelength resolution, nm
Δn	wall spacing within CFD
ΔT_{eff}	difference in effective average surface temperature, K
ε	surface emissivity
ε_λ	spectral emissivity
FIAT	Fully Implicit Ablation and Thermal Response code
FWHM	full width at half maximum
GRAM	Global Reference Atmosphere Model

h	Planck's constant: $6.626\ 10^{-34}$ J s
H	atomic hydrogen
H_2	molecular hydrogen
HDVS1	High Dispersion Visible Spectrograph No. 1, observation set up, Clay Center Observatory
HDVS2	High Dispersion Visible Spectrograph No. 2, observation set up, Clay Center Observatory
He	helium
IR	infrared wavelength region
IRIS	Intermediate Resolution Infrared Spectrograph, observation set up, Clay Center Observatory
k	Boltzmann constant: $1.38064\ 10^{-23}$ J K^{-1}
k	roughness height k, m
λ	wavelength, nm
L_λ	spectral radiance, W/(m^2 nm sr)
MPCV	Multi Purpose Exploration Vehicle
μ_w	viscosity at the wall, kg/m*s
N	atomic nitrogen
N^+	singly ionized atomic nitrogen
N_2	molecular nitrogen
N_2^+	singly ionized molecular nitrogen
NASA	National Aerospace …
NEQAIR	Non-Equilibrium Air Radiation line-by-line radiation code
NIR	near infra red wavelength region
NIRSPEC	observation set up in the near infrared, Utah State University
NO	nitric oxide
NO^+	singly ionized nitric oxide
O	atomic oxygen
O^+	singly ionized atomic oxygen
O_2	molecular oxygen
O_2^+	singly ionized molecular oxygen

Ω	solid angle, sr
Re_{kk}	Reynolds number evaluated at the roughness height k
ρ_w	density at the wall, kg/m^3
SRC	Sample Return Capsule
SCEBD	self-consistent effective binary diffusion model
T	temperature (if not specified otherwise translational), K
T_{eff}	effective average surface temperature, K
$T_{eff,548nm}$	effective average surface temperature for a Planck distribution, matching at 548nm, K
T_v	vibrational temperature, K
TPS	Thermal Protection System
QSS	Quasi Steady State
UTC	universal time
UV	ultra violet wavelength region
VIS	visible wavelength region
x	distance to the wall, m

I. Introduction

ON June 13, 2010, after a seven year journey to the asteroid Itokawa, the Japanese Hayabusa Sample Return Capsule (SRC) entered Earth's atmosphere at a speed of 11.7 km/s and was successfully recovered in the Woomera test range in Australia. Data on heat shield ablation and plasma characterization for this mission are very valuable for future sample return missions, e.g., from Mars, which will have similar hyperbolic entry speeds. There was, however, no instrumentation installed in the Hayabusa capsule to gather such data during reentry. Therefore, the reentry was studied by numerous imaging and spectroscopic instruments onboard NASA's DC-8 Airborne Laboratory in order to measure surface and plasma radiation generated by Hayabusa. The observatory flew above the clouds at an altitude of 12.5 km where absorption in the IR is already rather low. However, absorption through the ozone layer at altitudes between 25 km and 50 km prevented detection of radiation in the UV (i.e., below a wavelength of 300 nm).

A total of 19 experiments covered a wavelength range from 300 to 1600 nm in spectral resolutions from 0.1 nm to 10 nm [1] as illustrated in Fig. 1. A comparison with numerical simulation of data gathered with the Australian Ultraviolet Spectrometer AUS, the NIRSPEC experiments, and with the cameras *HDVS1*, *HDVS2*, and *IRIS* will be presented in Section IX due to their covereage of significant portions of the relevant wavelength range and time during the re-entry. In addition to the airborne experiments, ground-based observations from several sites were performed to obtain data for trajectory reconstruction [2].

The theoretical prediction of spectral radiation has to cover these different spectral ranges and resolutions for a comparison with experimental data. The solutions have to be tailored to the specific wavelength ranges and resolutions. Due to the large distance between the DC-8 and the Haybusa re-entry capsule (400 km to 100 km within the considered altitude range), Hayabusa appeared as a point source, and none of the experiments could provide spatial resolution of the capsule or the plasma layer. Consequently, a simulation of the radiation has to provide the integral over the whole flow field and the entire heat shield. In addition to the airborne experiments, ground-based observations from several sites were performed to obtain data for trajectory reconstruction through triangulation [2].

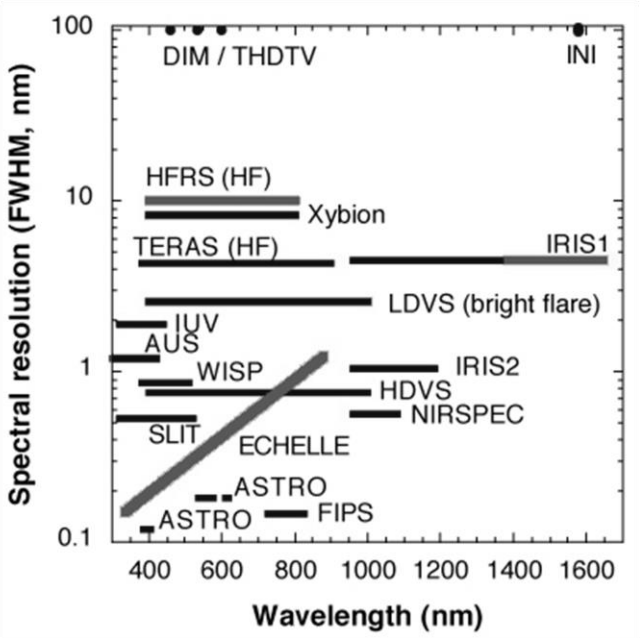

Fig. 1 Experiments, spectral ranges, and wavelength resolutions on the airborne Hayabusa observation campaign.

Before flight, computations of the flow field around the forebody were performed using the NASA in-house code *DPLR* [3, 4] at peak heating. The results were used as input for the material response code *FIAT* [5] to calculate

surface temperatures of the heat shield. Due to a lack of further specifications for the actual heat shield material, standard carbon phenolic was used in the simulation. The thermal radiation of the glowing heat shield was computed based on these temperatures and propagated to the predicted observation position. The radiation transport calculation required taking into account the influences of the observation angle and of atmospheric extinction to finally yield estimates of thermal radiation to be measured by the observing instruments during reentry. These estimates were used to provide calibration sources of appropriate brightness.

Post-flight, the flow solutions were recomputed to include the whole flow field around the capsule at 11 points along the best-estimated trajectory. Again, material response was taken into account to obtain the most reliable surface temperature information. These data were used to compute thermal radiation of the glowing heat shield and plasma radiation by the shock/post-shock layer system to support analysis of the experimental observation data. For this purpose, lines of sight data were extracted from the flow field volume grids and plasma radiation was computed using the Nonequilibrium Air Radiation code *NEQAIR* [6] which is a line-by-line spectroscopic code with one-dimensional transport of radiation. The procedure outlined here broadly followed an approach which had already been applied successfully to the analysis of the observation of the Stardust reentry [7]. However, the codes have since been significantly enhanced and most of the data handling procedures were changed and streamlined. Although the *NEQAIR* version used (*NEQAIR -2009 V7C*) provided an option for calculating surface radiation, discretization errors of the emitting surface area were encountered due to the practical limitation of the number of lines of sight originating from the surface. Therefore thermal radiation was computed separately directly on the grid used in computational fluid dynamics (CFD). However, *NEQAIR* computations were used to determine the absorption of surface radiation in the post shock layer system to be applied as correction to the separately computed thermal radiation. Formerly reported doubts about the results for bound-free continuum radiation in the *NEQAIR* computations [8] turned out to be relevant only if Boltzmann excitation was used for computing electronic state populations. When the quasi-steady state (QSS) assumption was used, the bound free continuum agreed reasonably with more sophisticated models [9], justifying the use of the *NEQAIR* model.

The process for predicting incident irradiance for instruments on board the flying observatory consisted of the following steps:

- Selection of suitable trajectory points and extraction of input data for *DPLR*
- Numerical simulation of the flow field data and radiation equilibrium surface temperatures with *DPLR*

- Post-processing of the *DPLR* data with the material response code *FIAT*
- Writing back the *FIAT* surface temperatures to the *DPLR* solution and re-converge the computation with a pointwise temperature distribution.
- Computation of Planck radiation emitted by the heat shield surface using the *FIAT* surface temperatures and effective radiating surface areas under the angle of view from the DC-8 position
- Extraction of lines of sight through the flow field
- Computation of plasma emission and radiative transport along these lines of sight with *NEQAIR*
- Propagation of the sum of thermal and plasma radiation to the DC-8 position using Hayabusa trajectory information and GPS data, and transformation into incident irradiance

The individual steps are described in the following sections and the resulting data are compared to the flight experiments.

II. Selection of Trajectory Points

Post-flight, the trajectory data were updated using the last known entry state vector as input to the trajectory code *Traj* [10, 11]. From these data, first estimates of stagnation point heat flux and velocity profiles were extracted to construct the heat pulse and then select appropriate time points on the pulse for CFD simulations. In addition to three CFD solutions at radiative, convective, and total peak heating, four points on each side of total peak heating were selected to cover the range where experimental data were available.

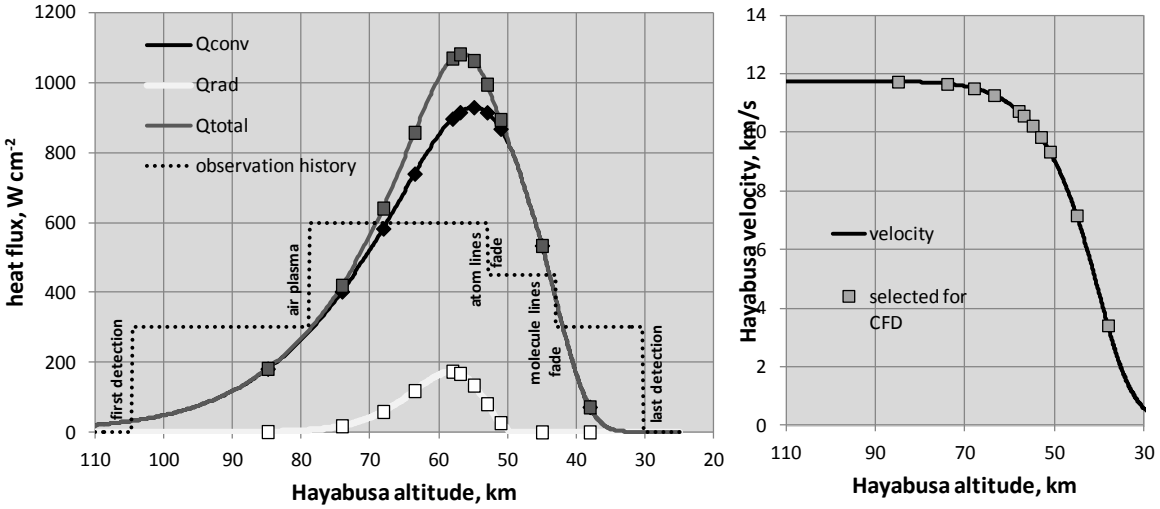

Fig. 2 Stagnation point convective, radiative, and total heat flux (left) and Hayabusa velocities (right) determined from trajectory data with engineering methods. The symbols mark the trajectory points selected for high fidelity CFD predictions (peak radiative, convective, and total heating are highlighted). The regimes where experimental data were gathered are shown.

Figure 2 shows the different heat flux values at the stagnation point predicted by *Traj*, the regions with measured data during reentry, and the points selected for high fidelity flow field simulations with *DPLR*, as well as the corresponding velocities vs. Hayabusa altitude. From trajectory and GPS data, the distances between Hayabusa and the DC-8 and the corresponding observation angles were obtained as shown in Fig. 3 together with the Hayabusa and DC-8 ground tracks on the map of the Woomera test range. For the observation, only the azimuth has to be taken into account since the elevation angle only tilts the plane in which rotational symmetry can be assumed for ballistic entries. The characteristic data for the different trajectory points are summarized in Table 1.

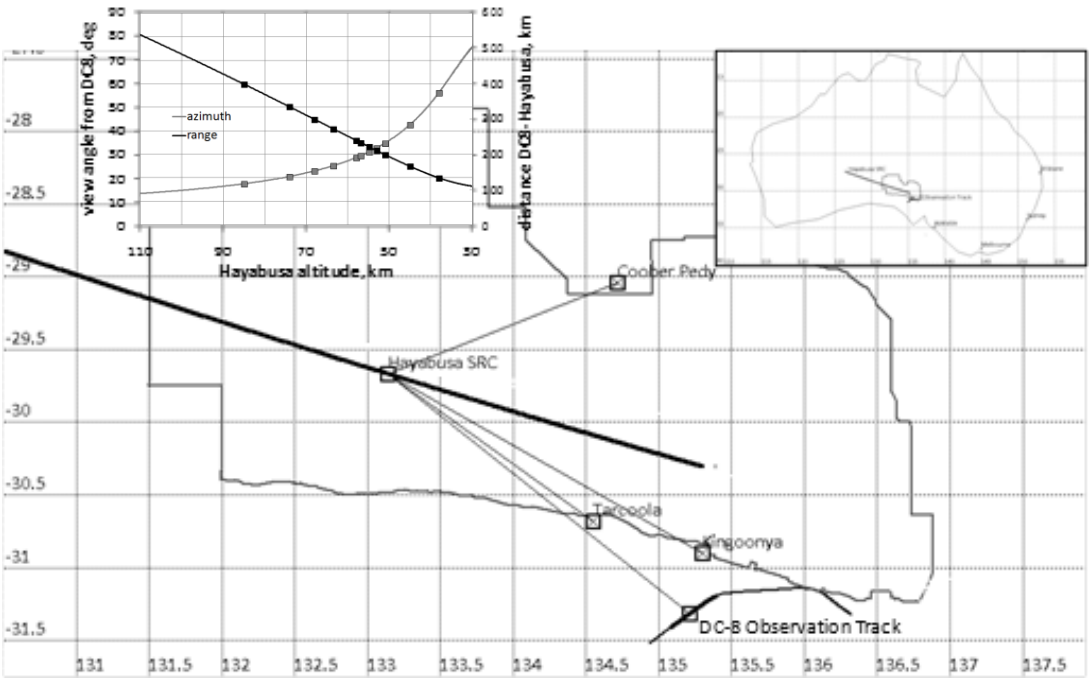

Fig. 3 Hayabusa (at 65 km altitude) and DC-8 ground tracks shown on a map of the Woomera test range, and distance between Hayabusa and DC-8 vs. Hayabusa altitude.

Table 1. Characteristic data for the selected trajectory points.

Simulation Point	UTC	Altitude km	Density kg/m^3	Velocity km/s	View angle deg	Range km	$T_{surf,stag}$ (*Traj* [10]) K
1	13:52:03.8	85	8.22E-6	11.7	17.5	398.9	1050
2	13: 52:09.6	74	4.96E-5	11.6	20.6	334.8	1816
3	13: 52:12.9	68	1.20E-4	11.5	22.9	299.3	2419
4	13: 52:15.4	63.5	2.18E-4	11.2	25.2	272.5	2839
5	13: 52:18.7	58	4.30E-4	10.7	28.6	239.9	3143
6	13: 52:19.4	56.9	4.92E-4	10.5	29.4	233.3	3167
7	13: 52:20.7	54.9	6.27E-4	10.1	31.0	221.5	3206
8	13: 52:22.0	53	7.91E-4	9.7	32.7	210.6	3199
9	13: 52:23.4	51	1.01E-3	9.2	34.7	199.1	3190
10	13: 52:28.4	45	2.12E-3	6.9	42.6	166.1	2961
11	13:52:37.6	38	5.51E-3	3.2	56.2	133.1	1991

III. Flow Field Simulation with *DPLR*

Environment Prediction Methodology

Because the vehicle trajectory was ballistic, axisymmetric calculations of the flow environment could be used. The aeroheating environment predictions were computed using *DPLR2D*, the two-dimensional/axisymmetric form of *DPLR* [3] v4.02.1. *DPLR* has emerged as one of NASA's workhorse flow solvers for aerothermal calculations, and it has been extensively validated with flight and tunnel data [12-13]. *DPLR* is a structured, finite-volume code that solves the reacting Navier-Stokes equations and models finite-rate chemistry and thermal nonequilibrium. Inviscid fluxes were computed using a modified Steger-Warming flux splitting [14] that achieves third-order accuracy using MUSCL extrapolation (monotone upstream-centered scheme for conservation laws) with a minmod flux limiter [15]. Viscous fluxes were computed with second-order accurate central differencing. Yos's mixing rule [16] was used to calculate viscous transport properties. Diffusion coefficients were calculated using the self-consistent effective binary diffusion (SCEBD) model [17]. The atmosphere was modeled using the 1990 version of Park's 11-species (N_2, N_2^+, O_2, O_2^+, NO, NO^+, N, N^+, O, O^+, e-), 19-reaction model [18]. Equilibrium constants were calculated using Gordon-McBride curve fits [19]. The flow was assumed to be in thermal nonequilibrium using Park's two-

temperature (T-T_v) model with T_e=T [18].A fully catalytic, radiative equilibrium boundary condition with ε = 0.85 as surface emissivity was applied at the vehicle surface.

Roughness-induced transition to turbulence was assessed with a correlation for Re_{kk}, the Reynolds number evaluated at the roughness height k. Figure 4 shows Re_{kk} along the axial length of the vehicle for all trajectory points selected for analysis. Re_{kk} is seen to increase as the vehicle travels deeper into the atmosphere. Since no roughness data for the Hayabusa heat shield were available, the post-flight estimate of maximum surface recession of 0.3mm [20] was used as an upper estimate of surface roughness. A critical value of 250 for Re_{kk} is assumed based on free flight experiments carried out in the NASA Ames Ballistic Range Facility [21]. The critical value was never reached for the trajectory points considered. Therefore, all cases were modeled as fully laminar.

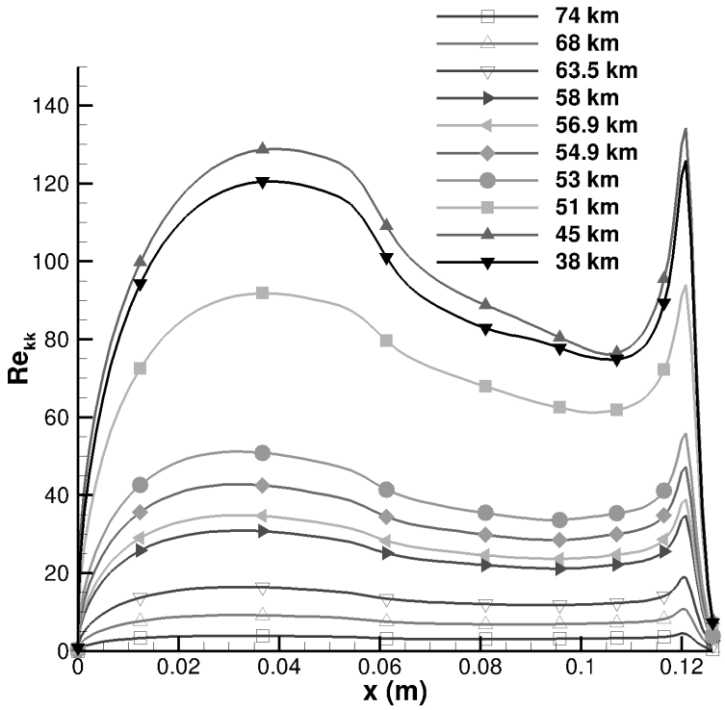

Fig. 4 Re_{kk} along heat shield centerline

The initial CFD grid was generated using *Gridgen* [22]. The generatrix curve defining the axisymmetric shape of the vehicle was extracted from a computer aided design file. The curve was discretized to capture regions of high surface curvature where large gradients in the flow were expected. The two-dimensional volume grid was then hyperbolically grown from the surface curve. The resulting grid (Fig. 5a), which was separated into forebody and aftbody blocks, contained 25,000 points with 121 points in the normal direction. This initial grid served as the basis grid for all CFD cases.

The large outer boundary would contain the bow shock and subsonic wake for all free stream conditions, but accurate aeroheating calculations require the outer boundary to be aligned with the bow shock and sufficient grid resolution at the wall to resolve the boundary layer. The *DPLR* flow solver provides such grid tailoring functionality. As part of the flow solution process, the basis grid is adjusted by aligning each grid outer boundary with the bow shock and changing the wall spacing Δn to maintain a cell Reynolds number of 1. The cell Reynolds number is defined as

$$\mathrm{Re}_{cell} = \frac{\rho_w a_w \mu_w}{\Delta n} \tag{1}$$

where all quantities are taken at the wall. An example of a final tailored grid is shown in Fig. 5b.

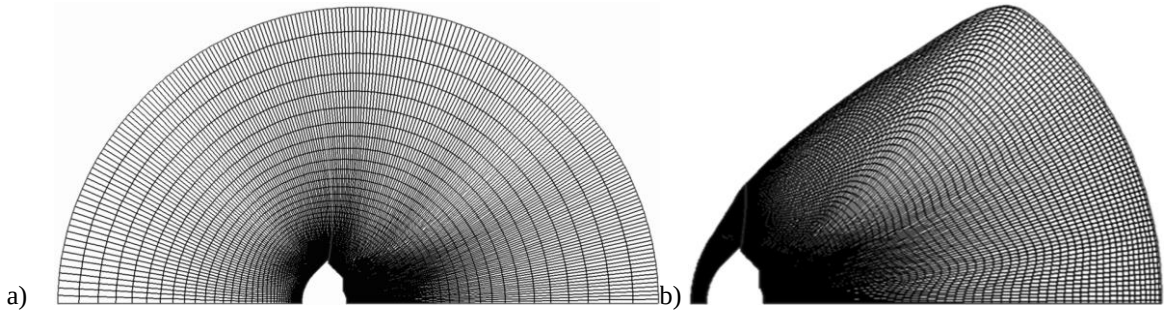

Fig. 5. a) hyperbolic grid and b) tailored grid.

Eleven points along the trajectory were initially chosen for CFD computations in order to span the heat pulse. Convergence proved difficult for the first point chosen at an altitude of 85 km and a velocity of 11.7 km/s. Upon further investigation, the freestream Knudsen number, defined as the ratio of the mean free path to a reference length (in this case the vehicle diameter) at this condition was found to be 0.044. Continuum flow solvers such as *DPLR* are only applicable for flows with Knudsen number less than 0.01. Therefore the case at 74 km and 11.6 km/s velocity became the highest altitude point, the Knudsen number for this case being 0.0081. For the remaining ten cases, the free stream conditions were initially provided as velocity-altitude pairs from the best estimate trajectory. In a first approach, the free stream values needed for CFD calculations, atmospheric temperature and density, were defined by the U.S. Standard Atmosphere 1976 [23].However, the more sophisticated Global Reference Atmosphere Model (GRAM) [24] predicted atmosphere densities higher by about 10% for the given latitude of the re-entry. Therefore, the final computations were done using the GRAM 99 atmosphere model.

Sample CFD Solution

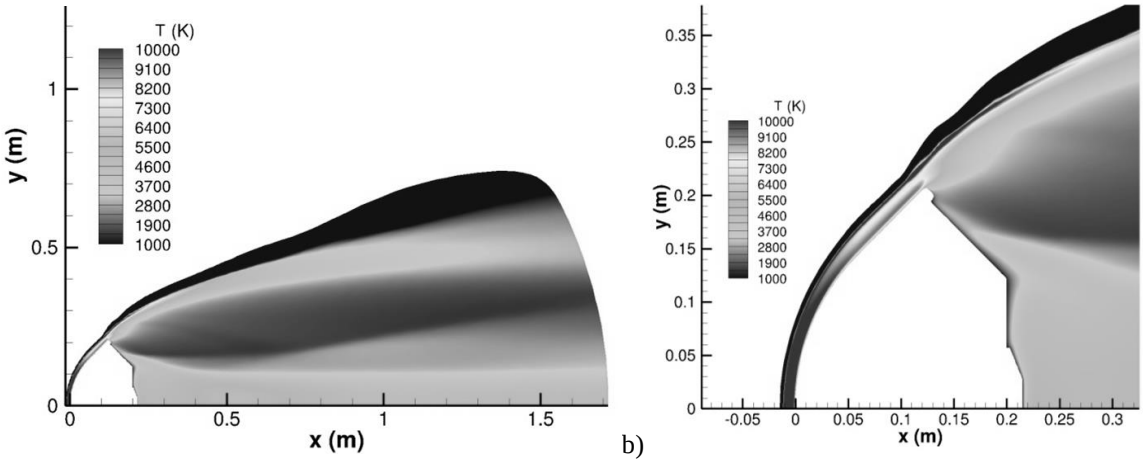

Fig. 6 **a) Fullbody temperature contours for laminar, 56.9 km solution**

b) Forebody temperature contours for laminar, 56.9 km solution

A representative laminar flowfield solution (peak total heating at 56.9 km) is presented in Fig. 6. The temperature contours show that the grid outer boundary alignment allows for the capture of the sharp bow shock. The temperatures behind the shock are around 10,000 K and the temperatures in the wake are around 5,500 K.

As previously stated, *DPLR* is capable of modeling thermal nonequilibrium through a two temperature model [18]. The post-shock translational (T) and vibrational (T_v) temperatures and the species number densities along the stagnation line for selected trajectory points are shown in Fig. 7. In the shock itself and in the region immediately behind the shock the plasma is in thermal nonequilibrium. The translational temperature in this region overshoots to values up to 20,000 K. Most of the post-shock region, however, is in equilibrium.

The species present in the freestream, molecular Nitrogen and Oxygen, mostly dissociate in the high temperature region behind the shock. Of the eleven constituent species present in the gas model, the species with the highest number densities in the post shock region are atomic Nitrogen and Oxygen, ions of Nitrogen and Oxygen, and electrons.

74km

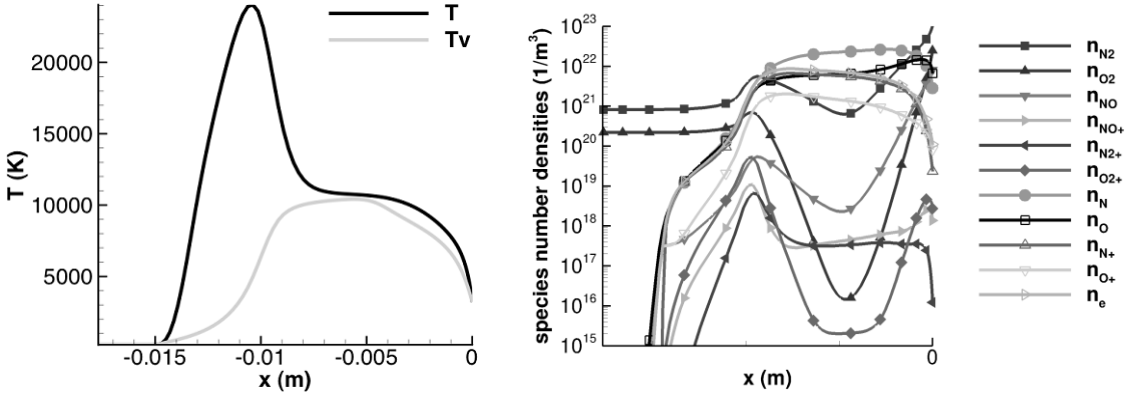

58km

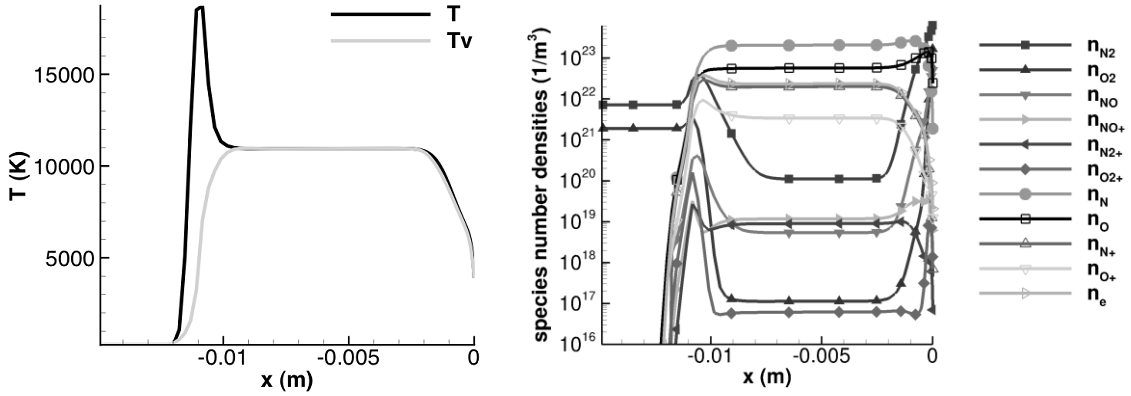

54.9km

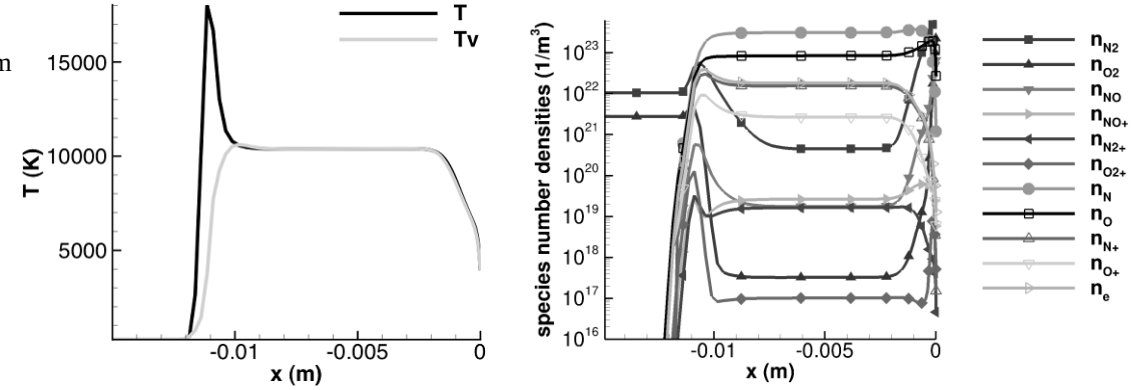

51km

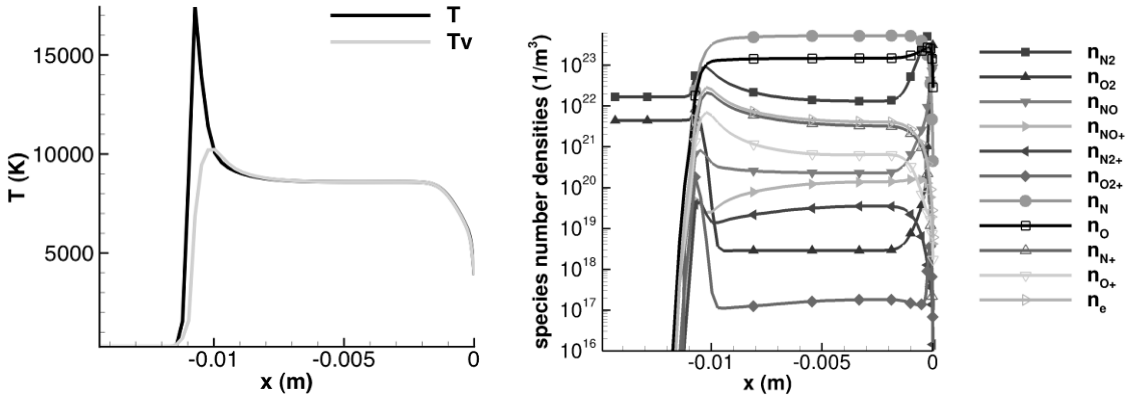

Fig. 7 Translational and vibrational temperatures and species number densities along the stagnation line at altitudes of 74 km (start of the computational regime), 58 km (peak radiative heating), 54.9 km (peak convective heating), and 51 km.

IV. Extraction of Lines of Sight through the Flow Field

The procedure for extracting lines of sight through the flow field under a certain view angle was originally developed for the analysis of the Stardust Reentry Observation Campaign [7]. For a ballistic entry, rotational symmetry can be assumed for this computation and only a half body has to be computed, the symmetry plane being defined by the capsule axis and the view angle vector. First, the rotationally symmetric 2D flow field solution obtained by *DPLR* was transformed to a 3D grid by rotating the 2D data. Then, a uniform 2D orthogonal grid perpendicular to the view angle vector was created behind the flow field. From each element of this grid a line of sight was generated parallel to the view angle vector and tracked through the flow field. The "inner" lines intersect the Hayabusa body at two points. The downstream parts of these lines are shadowed by the capsule and were omitted from further computation. The parts in front of the capsule do contribute to the visible emission and are transferred as lines of sight to be used as input for the spectral computation. The "outer" lines do not intersect the capsule surface and are entirely visible. Moreover, due to low temperatures and densities, the wake behind the capsule does not contribute significantly to the radiation. To ensure a sufficient spatial resolution of the "hot" regions with high gradients, a cut-off plane is placed behind the capsule to define a common starting position for all outer lines. For the current computations, this plane was placed 0.1 capsule lengths behind the rear surface. To determine the sensitivity, a test computation was performed with the cut-off plane placed one capsule length behind the rear surface with no significant change of the resulting spectra. Since only a half body was computed, the sum of all lines yields half the emitted radiation. Figure 8 illustrates the process of extracting the lines of sight and shows selected lines of sight obtained with this process for altitudes of 74 km and 53 km at view angles of 20.6 deg and 32.7 deg, respectively.

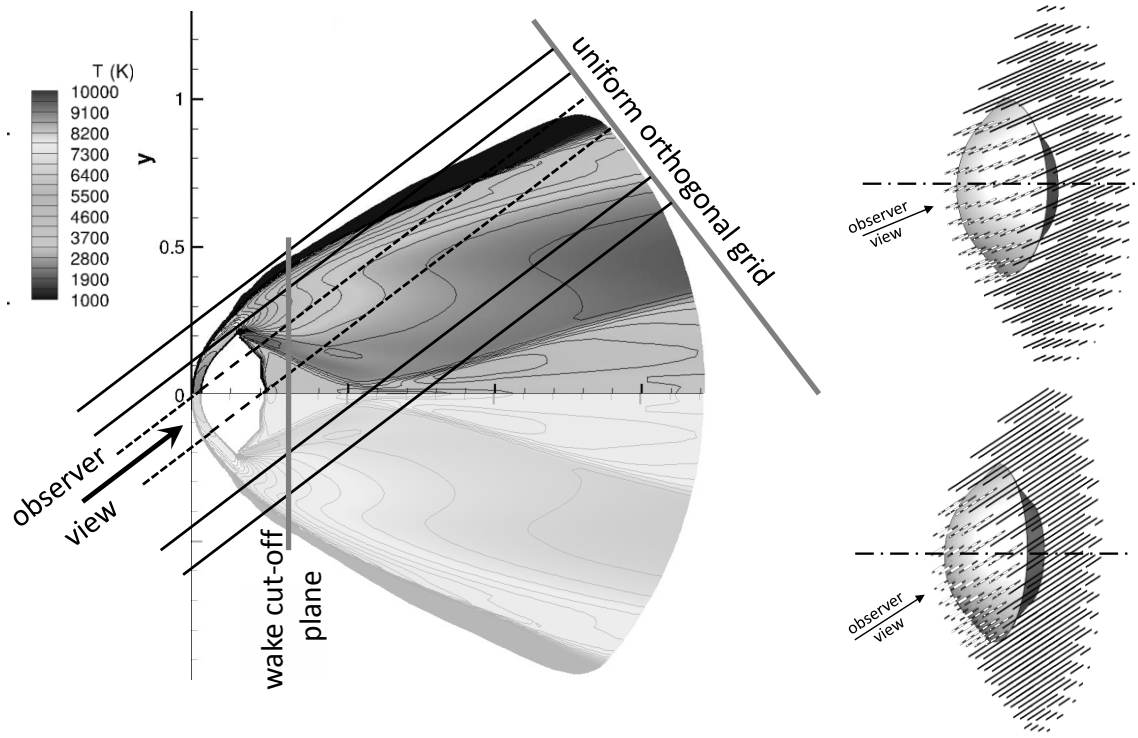

Fig. 8 Illustration of the extraction process for the lines of sight and examples for Hayabusa altitudes of 53 km and 74 km. Dotted lines show an intersection with the capsule (inner lines), solid lines solely pass through the plasma region (outer lines).

The number of lines is controlled by the spacing of the uniform orthogonal grid. A sensitivity study was performed at an altitude of 58 km with 49, 99, 149, and 199 grid elements in each direction. The integrated emission showed significant dependence up to 149^2 elements, though increasing to 199^2 elements altered emission by less than 1%. Therefore, all computations were performed on the grid with 149^2 elements yielding between 443 and 620 inner and between 662 and 850 outer lines in the altitude range from 45 km to 74 km. Each line covered a spatial cross section between 1.16 and 1.04 cm^2.

V. Computation of Plasma Radiation

The Nonequilibrium Air Radiation (*NEQAIR*) code [6] is a line-by-line radiation code that computes the emission and absorption spectra (along a line-of-sight) for atomic and molecular species, including both electronic and vibrational (infrared) band systems. Individual electronic transitions are evaluated for atomic and molecular species. The code can model the bound-free and free-free continuum radiation caused by interactions of electrons with neutral and ionized atomic species. Line broadenings due to Doppler, Stark, resonance, and Van der Waals broadening as well

as the natural line width are included in the code through Voigt broadening. Additional broadening (e.g., instrument broadening) can be included in a post-processing scan function, usually in the form of a Voigt line shape. Planck radiation from a glowing surface can be computed as grey body radiation with a given emissivity.

The radiative emission is computed along each line of sight which is divided into a series of one-dimensional cells, and the radiative emission, absorption, and specific intensity are computed at every line-of-sight cell. The radiative heat flux on a surface can be determined using either a tangent slab or spherical cap assumption. *NEQAIR* is capable of simulating the emission of a variety of species such as atoms (N, O, H, C, He) and molecules (N_2, N_2^+, NO, O_2, H_2, CO, C_2, CN). For the present Hayabusa analysis only O, N, N_2, N_2^+, and O_2 were used due to the limitations of the accessible wavelength range towards the UV and the fact that ablation products in the flow field were not modeled by *DPLR*.

Test computations with one line of sight were conducted to determine the necessary wavelength resolution of the initial spectra. The results were found to be insensitive to a further reduction beyond a wavelength spacing of 0.01Å. These initial spectra were integrated during the computation process yielding the total radiation of the flow field. In addition, low resolution spectra were generated for each line of sight using the internal scanning procedure of *NEQAIR* and integrated after the set of computations was finished. The integrated high resolution spectra were used for the radiation transport calculations. The resulting irradiance spectra at the DC-8 position were then broadened to values individually tailored to the different experimental resolutions.

In general, non-equilibrium radiation is expected from the region immediately behind the shock when the thermodynamic state is in the process of adapting to the instantaneous increase in temperature and pressure in the shock. Within the stationary plateau behind the shock, Boltzmann distributions should dominate the electronic excitation as soon as the pressure and ionization fraction are high enough to provide a sufficient number of electron collisions for the equilibration of the excited states. The nonequilibrium regions of the flow will show significant deviations from a Boltzmann distribution of the electronically excited states. These regions are covered by a quasi-steady state (QSS) assumption [18] which is implemented in *NEQAIR*. The QSS solution converges with sufficient accuracy to the Boltzmann solution when equilibrium conditions are reached. Therefore, the whole flow field is computed with the QSS assumption.

During initial computations [8], significant differences between the Boltzmann and QSS computations were seen in the level of continuum radiation. With Boltzmann, bound-free continuum values on the order of the molecular bands

were found [8]. For the present computations, however, only QSS modeling was used. With QSS, the bound-free values agree reasonably with a more sophisticated model [9].

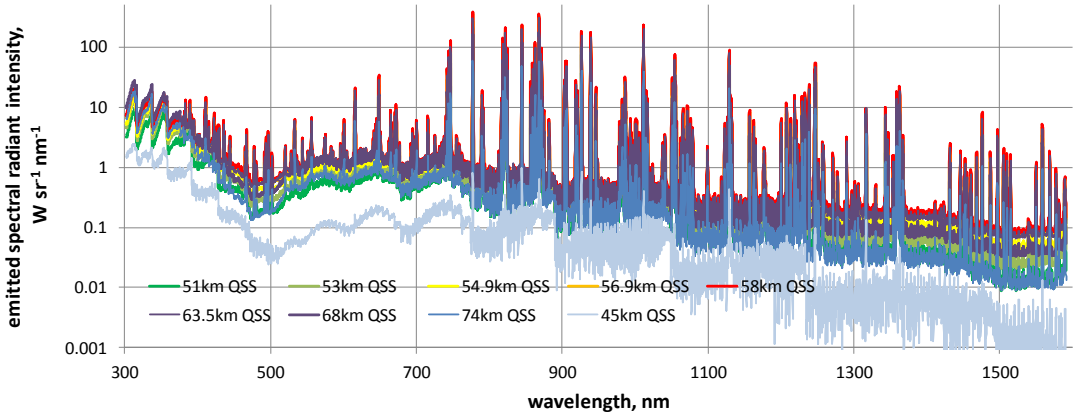

Fig. 9 Integrated plasma spectra under the assumption of QSS populations of the electronically excited states.

VI. Propagation of Emitted Radiation to the DC-8 Position

The final step to be able to compare the simulated spectra with experimental data is the propagation of the emitted radiation to the observer's position (i.e., the DC-8 position). Both plasma and surface radiation are computed in spectral radiance values, i.e., power per emitting surface area, wavelength interval and solid angle in the units W m^{-2} nm^{-1} sr^{-1}. Along the trajectory, the effective emitting surface changes due to the changing view angle and the solid angle will vary with the distance to the observer. Therefore, a calibration of the instruments to spectral radiance cannot be performed in a straightforward way, and the calculated emitted radiance has to be converted to spectral irradiance (received spectral power per receiving surface area in the units W m^{-2} nm^{-1}). For this purpose, all computed spectral radiance values were converted to a spectral radiant power in W/nm by multiplying with the emitting surface and the solid angle in which radiation is emitted (compare Fig. 10) and then divided by the receiving surface area given by the smallest aperture in the detection set-up. (The aperture diameter finally cancels out since it is used both for the solid angle and the receiving surface.)

The needed quantities are: the Hayabusa-DC-8 distance, the view angle from the observer to Hayabusa, and the emitting surface area. The first two quantities are obtained from trajectory data, while the third is either the grid cell for the plasma or the projected area of the Hayabusa surface element for thermal radiation. A similar procedure was applied for the calibration sources.

The detected radiation was partly absorbed by the atmosphere. During pre-flight analysis the atmospheric extinction was computed with *MODTRAN* [28] for different Hayabusa altitudes as shown in Fig. 11. The main influence of air absorption takes place at wavelengths below 700 nm and at the absorption bands of water and oxygen around 628 nm, 687 nm, 760 nm, 935 nm, 1130 nm and in the mid infrared. The changes in transmission with altitude were moderate in the visible and mid-infrared and stronger in the ultraviolet region.

Within the range of interest, the observation distance "as flown" was lower by an average of about 5%. However, since the change in atmospheric transmission with Hayabusa altitude (and therefore with observation distance) is generally weak, this difference does not cause significant changes in transmission.

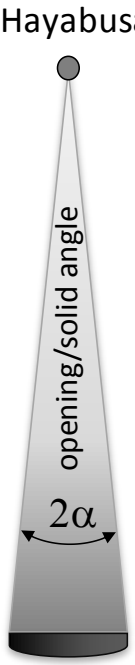

$$\Omega = 2\,\pi\,(1-\cos(\alpha))$$

Fig. 10 Illustration of the solid angle for propagation of Hayabusa radiation to the DC-8.

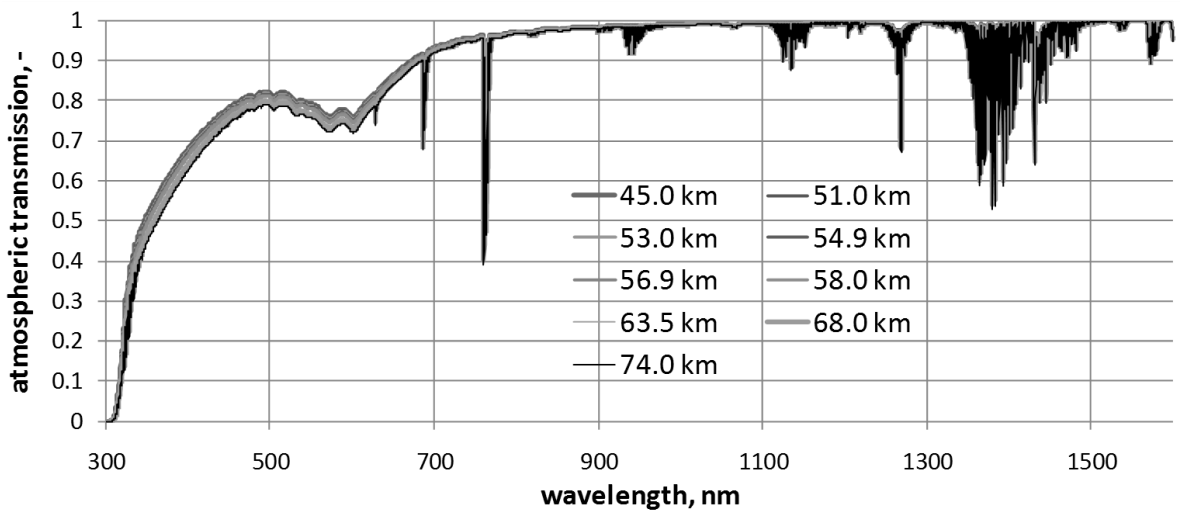

Fig. 11 Atmospheric transmission vs. wavelength for different Hayabusa altitudes (pre-flight) computed with *MODTRAN* [28].

VII. Material Response Computation with *FIAT*

FIAT is an implicit ablation and thermal response program for simulation of one-dimensional transient thermal energy transport in a multilayer stack of isotropic materials and structure which can ablate from a front surface and decompose in-depth [5]. The governing energy balance is basically a transient thermal conduction equation with additional pyrolysis terms. A three-component internal decomposition model is used. Figure 12 illustrates inputs and outputs to and from *FIAT*.

For the current analysis, heat flux values and radiation equilibrium temperatures from the *DPLR* computations as well as radiative heat flux values derived from *NEQAIR* computations at 20 points distributed along the arc length of the Hayabusa heat shield were used as input for the *FIAT* runs.

FIAT accounts for the effect of mass injection through a blowing reduction factor [5]. Therefore, the *DPLR* solution was computed with a fully catalytic non-ablating surface assumption, and it is not necessary to account separately for mass injection.

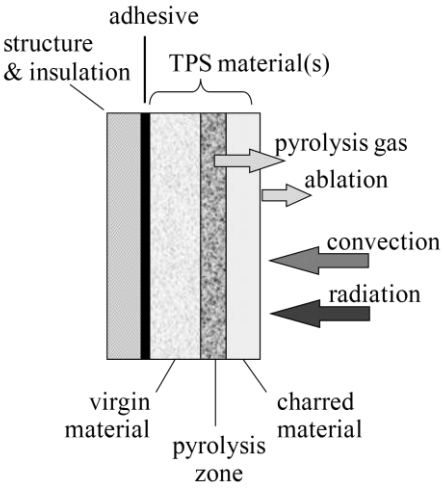

Fig. 12 *FIAT* working principle.

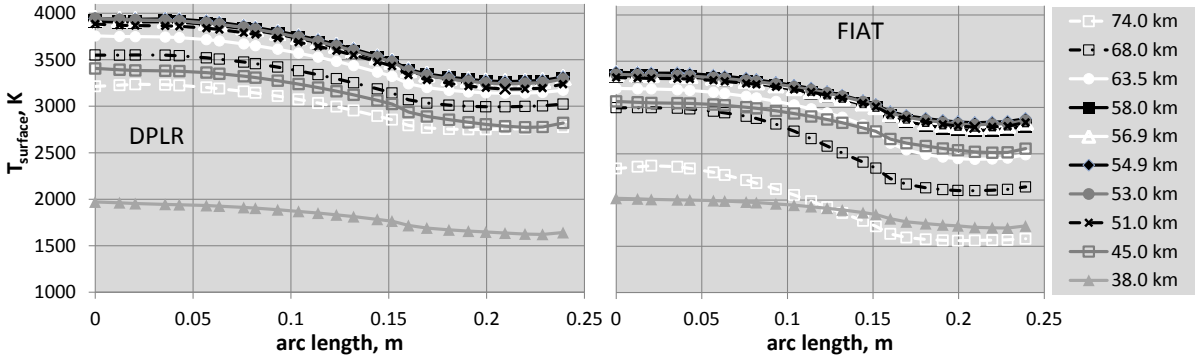

Fig. 13 Hayabusa surface temperatures from *DPLR* (radiation equilibrium) and after material response computation with *FIAT*.

Around peak heating, the material response results yield a surface temperature decrease due to ablation by about 500-600 K compared to the radiation equilibrium solution with a maximum value of 3,380 K at the stagnation point as shown in Fig. 13.

VIII. Computation of Thermal Radiation of the Heat Shield

As seen during the Stardust observation, a major part of the emitted radiation is thermal emission from the glowing heat shield. This radiation is computed as Planck radiation:

$$L_\lambda(T) = \varepsilon_\lambda \frac{2hc^2}{\lambda^5} \frac{1}{\exp\left(\frac{hc}{\lambda kT}\right)-1}$$

An emissivity value of 0.9 (charred carbon phenolic) was used. The spectral radiance has to be integrated over the surface area to obtain the total radiation observed. Since the capsule approaches the observer, the view angle to the surface changes continuously as already shown in Fig.3. For the surface radiation, only the projected area can be used due to Lambert's Law. For a computation of the projected area, a FORTRAN code originally developed for the Stardust observation [7] was applied to the Hayabusa forebody.

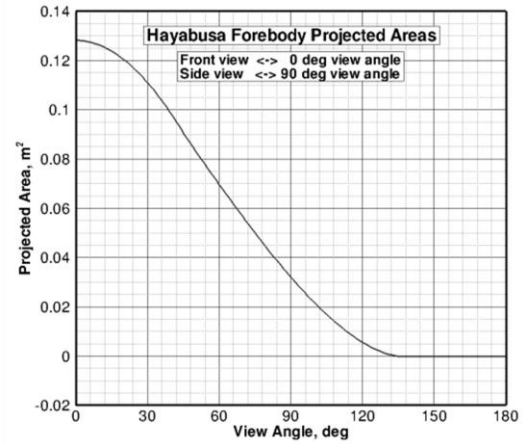

Fig. 14 Hayabusa forebody projected areas vs. view angle.

The back shell was assumed to emit only negligible contributions to the total radiation. Figure 14 shows the total visible surface area as a function of the view angle. Due to the capsule shape, the front surface is visible to an angle of about 130 deg until the back shell completely blocks the forebody.

If the capsule were to have a constant surface temperature, this total projected area could be used for the computation of thermal radiation. If temperature gradients occur, this essentially means that the total thermal radiation is a superposition of a number of different Planck functions multiplied with the corresponding radiating area. In the simulation, this was realized by computing the projected areas on the CFD surface grid resolution for each circular ring of cells (which, due to rotational symmetry, is defined to be at one temperature).

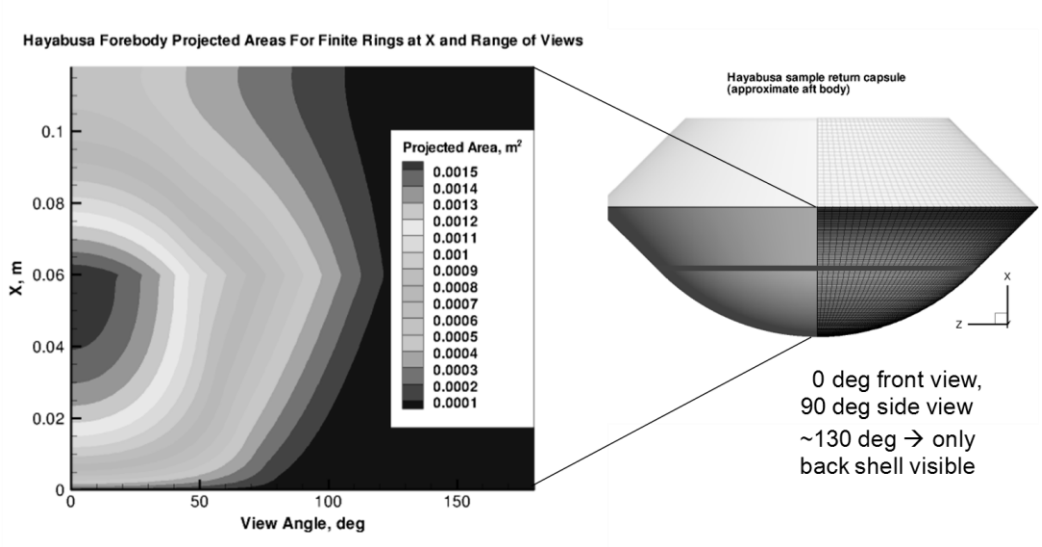

Fig. 15 Hayabusa forebody projected areas for finite rings (shown in red for one particular axial position) vs. view angle.

This computation of surface radiation as described above, however, does not include absorption of the thermal radiation in the post-shock plasma. Although *NEQAIR* has the capability of computing surface radiation, for the given number of lines of sight, the emitting surface area in the *NEQAIR* computations was over-predicted by about 10%, thereby over-predicting the total radiation from the surface. Increasing the number of lines of sight until the surface area was reached with sufficient accuracy would have caused a significant increase in computational effort while not significantly changing the plasma emission (compare section IV). Therefore, *NEQAIR* was used for computing the absorption of surface radiation in the shock layer system as a correction to the above described procedure for computing the surface radiation. Computations with and without surface radiation were conducted for optically thin and for absorbing cases. From these computations, the absorption of surface radiation in the post-shock plasma was determined as shown in Fig. 16. The maximum spectral absorption is on the order of 6% and occurs at the spectral positions of atom line emission. Therefore, in the resulting spectra the absorption of thermal radiation appears as a reduction of the atom line emission. The total surface radiation between 300 nm and 1.6 μm changes through absorption by no more than 0.05% at most.

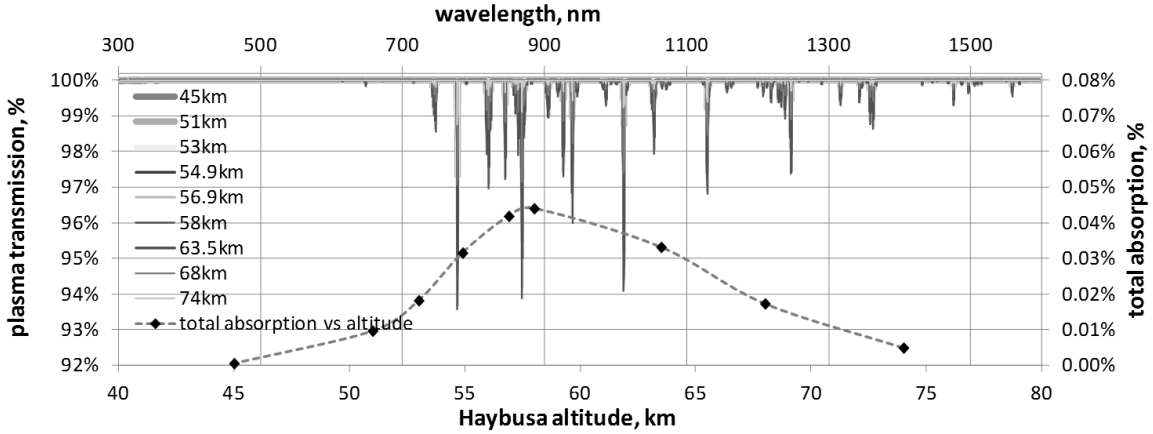

Fig. 16 Spectral absorption of surface radiation in the Hayabusa flow field vs. wavelength, and maximum total absorption of thermal radiation between 300nm and 1.6μm vs. Hayabusa altitude.

IX. Incident Spectra at the DC-8 Position and Comparison with Preliminary Experimental Data

In Fig. 17, the thermal radiation emitted by the Hayabusa heat shield is plotted vs. wavelength as incident irradiance at the DC-8 position but not yet corrected for atmospheric transmission. Although the temperatures at peak heating are higher than afterwards (compare Fig. 13), the observed thermal radiation peaks at 51 km Hayabusa altitude due to the decreased distance to the capsule and increased solid angles.

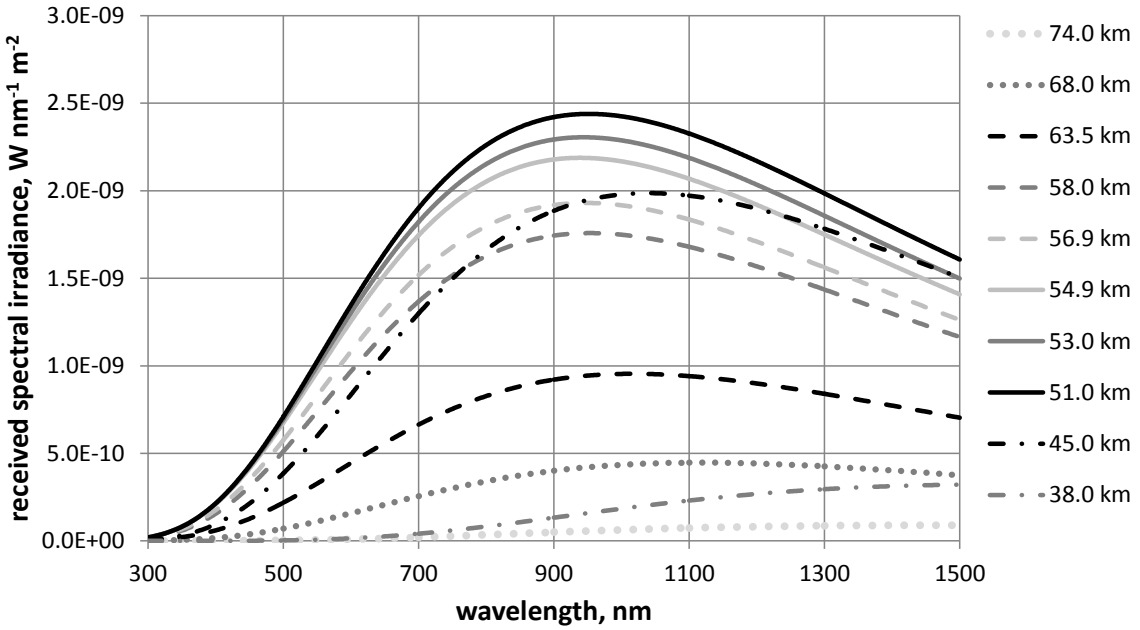

Fig. 17 Thermal radiation emitted by the glowing heat shield after material response without corrections for atmospheric transmission.

Thermal radiation between 58 km and 45 km varies but remains at about the same order of magnitude. Between 45 km and 38 km, a steep decrease of thermal radiation is seen. Recent NASA studies [29,30] made attempts to quantify the uncertainty of the numerical simulation, e.g., for the studies performed in the frame of the CEV (now MPCV) vehicle. For these conditions, uncertainties in computed heat fluxes on the order of ±25% were found which translate to a surface temperature uncertainty of about ±6%. If the same values are applied to the Hayabusa re-entry, modeling uncertainties of about +(33-43)% and –(27-34)% are obtained for the thermal radiation.

If experimental spectra are analyzed independently from the theoretical analysis, often a constant surface temperature of the heat shield is assumed since none of the experiments can provide measurements in spatial resolution. To support these interpretations, an attempt at defining an effective surface temperature was made to find a single temperature which would represent the incident thermal radiation at the DC-8 position.

In a first approach, a temperature was determined that produced the same amount of thermal radiation in the total wavelength range under investigation from 300 nm to 1600 nm as the *DPLR* temperature distribution for each given geometric situation (i.e., view angle, effective surface area, distance between Hayabusa and DC-8, and atmospheric transmission). Indeed, such temperatures T_{eff} reasonably rebuild the Planck radiation using the *FIAT* temperature distribution for altitudes of 58 km and below. Above 58 km, the spectral shape of the solutions with only one effective temperature did not adequately reproduce the spectral shapes shown in Fig. 17.

These results seem reasonable since the gradient of surface temperature decreases with sinking altitude as depicted in Fig. 13. However, most experiments cover only a limited wavelength range. Therefore, an additional effective temperature $T_{eff,548nm}$ was determined for which the thermal radiation at 548 nm (peak of the Johnson V band [31] at the center of the visual range) agrees with the predicted irradiance. $T_{eff,548nm}$ is typically higher than T_{eff} although the difference decreases with sinking altitude. Both effective temperatures and their difference are depicted in Fig. 18 vs. Hayabusa altitude.

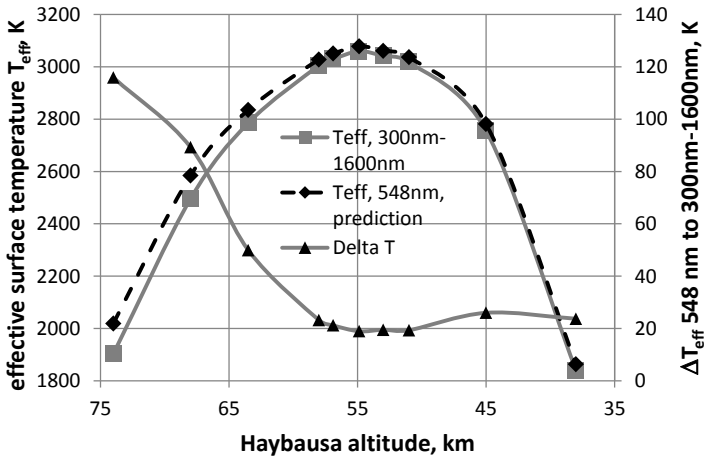

Fig. 18 Effective average surface temperatures determined from the sum of thermal radiation between 300 nm and 1.6 μm and at 548 nm.

The final comparison with experimental data has to be done with the superposition of thermal and plasma radiation multiplied by the atmospheric transmission. The results are shown in Fig. 19. For a comparison with experiments without spectral resolution such as regular cameras (or tracking cameras), the spectral irradiance has to be integrated over wavelength. For the data shown in Fig. 20, this was done in the wavelength range between 300 nm and 1,600 nm. To compare to a given instrument, however, this calculation needs to incorporate the spectral response function of that instrument.

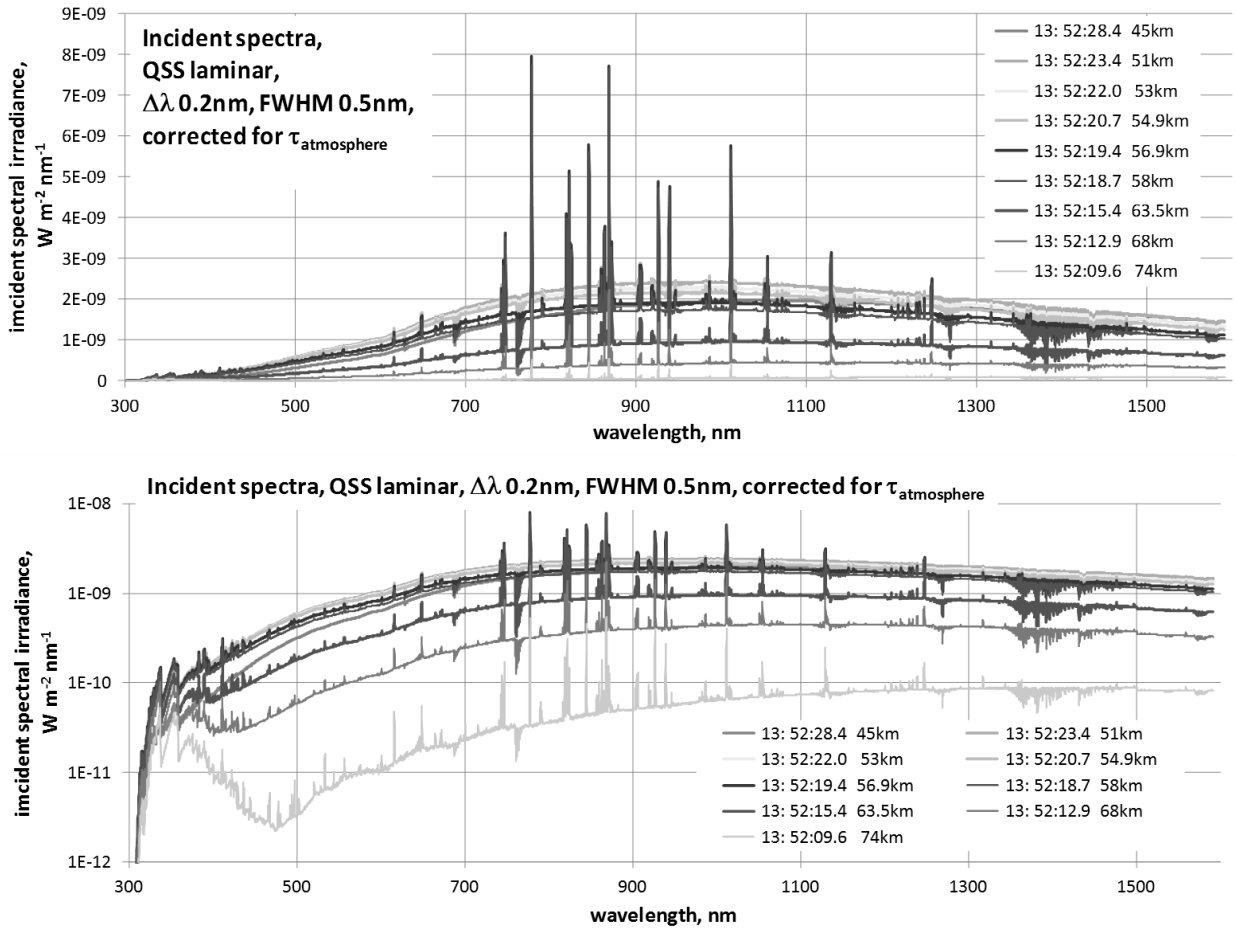

Fig. 19 Combined computed incident spectra at the DC-8 position on linear (top) and log (bottom) scales.

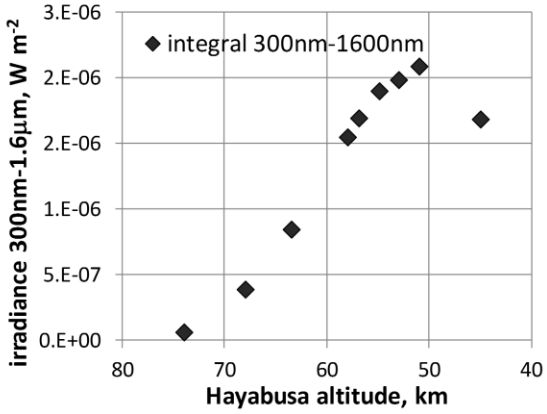

Fig. 20 Irradiance integrated between 300 nm and 1600 nm for comparison with experiments without spectral resolution (e.g., tracking cameras or 0 order of transmission grating set-ups).

Comparison with Experimental Data:

Calibrated data were available from the Australian Ultraviolet Spectrometer AUS [32] in the UV shortly after peak heating, from the NIRSPEC experiments [34], operated by Utah State members, before and around peak heating, and from the cameras *HDVS1* (High Dispersion Visible Spectrograph No. 1), *HDVS2* (High Dispersion Visible Spectrograph No. 2), and *IRIS* (Intermediate Resolution Infrared Spectrograph), (data available throughout the whole observation period), operated by Clay Center Observatory team members.

AUS measured spectrally resolved data ($\Delta\lambda$ = 0.187 nm, FWHM ~0.75 nm) between 300 nm and 470 nm. The main radiator in this wavelength region is CN which, due to the limitation in the simulation tools, unfortunately could not be simulated in the CFD analysis as it is a product of ablation. Therefore, the main molecular bands could not be included in the simulated spectra. Weaker radiators are N_2 and N_2^+ emission as well as a clearly recognizable continuum. Data were available at 13:52:22.40 UTC which is in between the simulated altitudes at 51 km and 53 km after peak heating.

The continuum portions of the experimental spectra are in excellent agreement with the prediction as shown in Fig. 21 and clearly lower than the former predictions of turbulent flow [8]. This confirms the initial assumption of a laminar flow throughout the whole trajectory. The agreement with the emission of the N_2/N_2^+ system is good. Further experimental data at altitudes closer to peak heating would be needed for more precise statements.

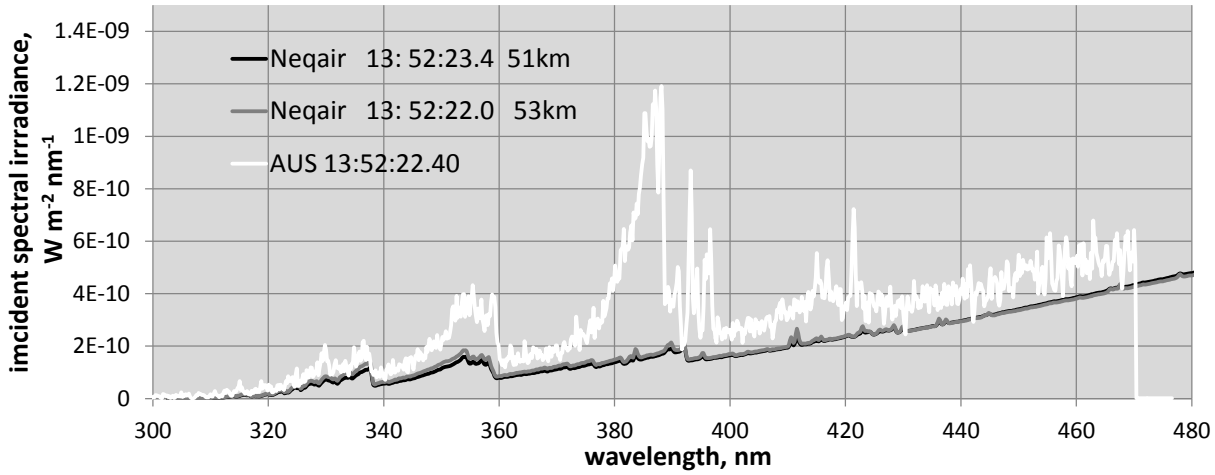

Fig. 21 Comparison with preliminary experimental data in the UV measured with the AUS instrument at altitudes after convective peak heating [32].

NIRSPEC measured spectrally resolved data ($\Delta\lambda$=0.286 nm, FWHM 1.4 nm) between 960 nm and 1080 nm. The strong lines seen in this spectrum are nitrogen multiplets. Data between 13:52:11.1 UTC and 13:52:19.9 UTC

corresponding an altitude range from 72 km to 56 km Hayabusa altitude were available, the latter being shortly after peak heating at 56.9 km.

The best agreement, both in terms of spectral features and intensity, can be seen between the simulation at 68 km altitude and the measured spectrum at 13:52:15.4 UTC. This, however, would correspond in a time shift of 2.5 s between simulation and experiment which is well outside the time uncertainties of both simulation and experiment. At corresponding times, the simulation is always higher than the experiment. Close to peak heating, and over-prediction of about 30% can be seen in both continuum and atom lines.

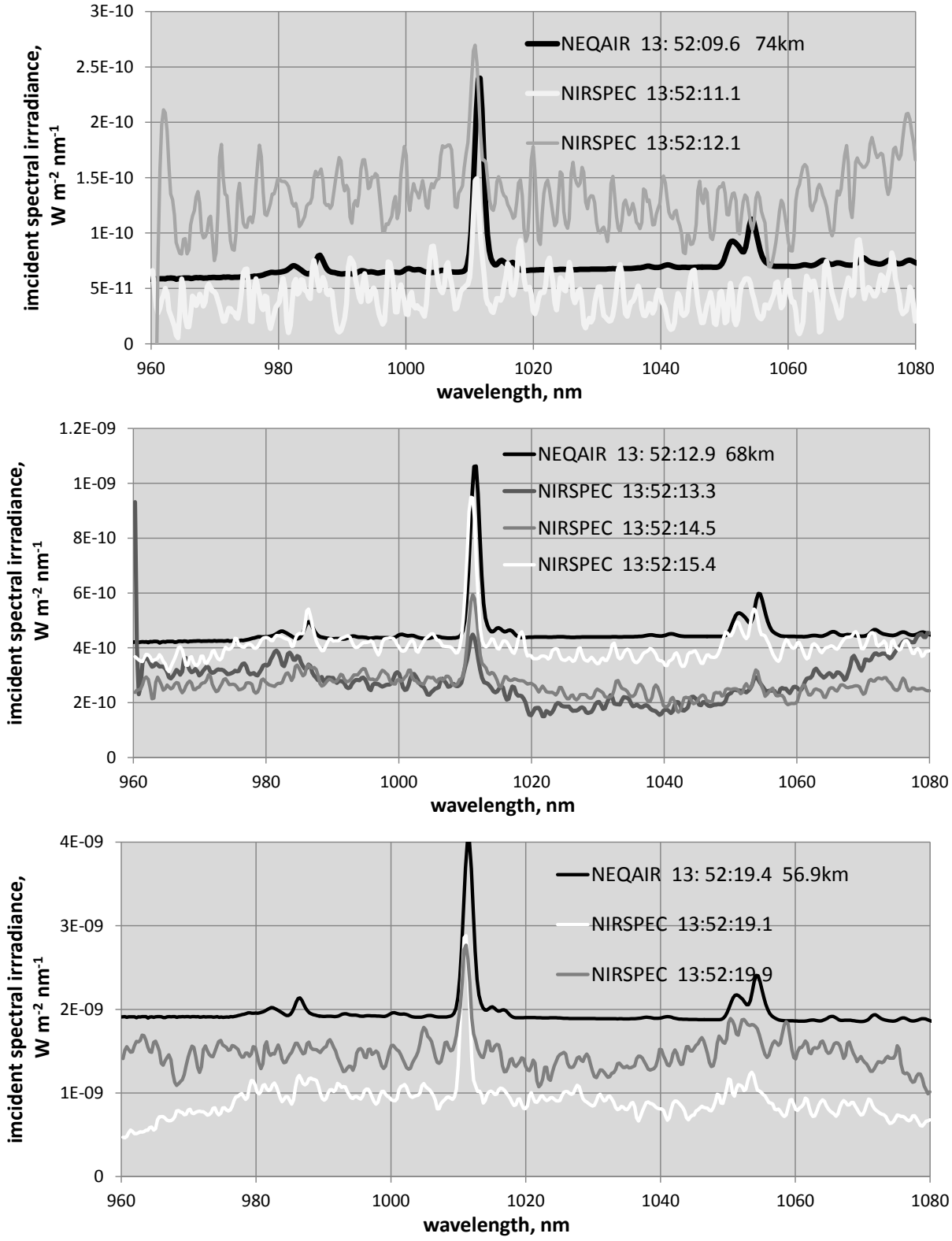

Fig. 22 Comparison with experimental data measured with the NIRSPEC instrument compared to *DPLR/FIAT/NEQAIR* simulation at altitudes between 74 km and 56.9 km [34].

The combination of HDVS1, HDVS1, and IRIS provided spectra from 400 nm up to 1,300 nm with spectral resolutions between 0.5 nm and 1.2 nm at the focused points. In Fig. 23, overview spectra around the simulation altitudes of 68 km, 58 km and 51 km are presented.

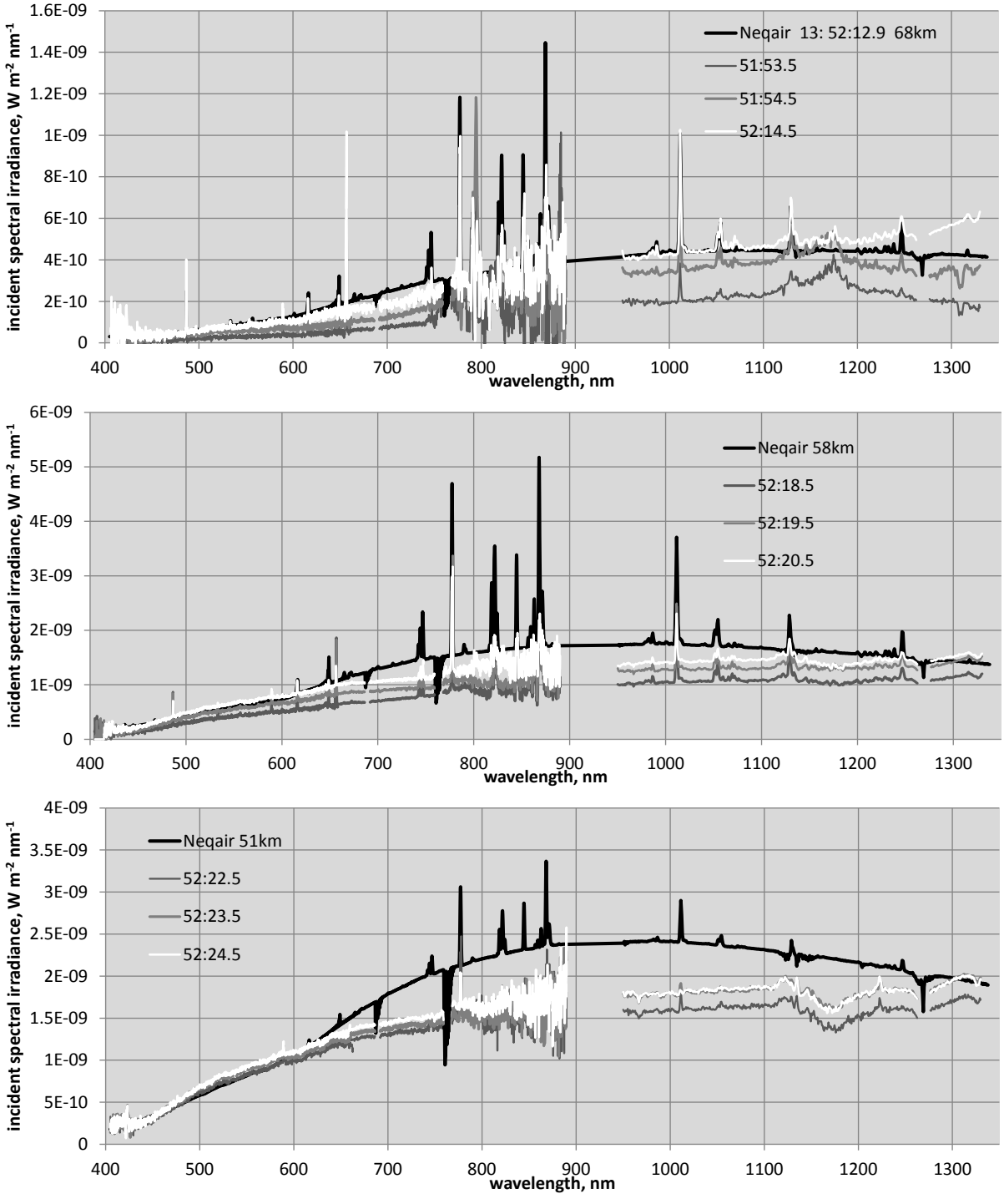

Fig. 23 Comparison of NEQAIR simulation with experimental data from 400 nm to 1,300 nm combined from data gathered with the HDVS1, HDVS2, and IRIS instruments at altitudes of 68 km, 58 km, and 51 km [1].

At high altitudes, the simulation is always higher than the experimental data unless a time shift of about 2.5 seconds towards lower altitudes is assumed, as seen before. However, both the uncertainty estimates of the trajectory simulation and the time synchronization during the experiments are on the order of the camera frame rate and thus significantly lower than this delay.

At altitudes of 58 km and below, the experimental spectra are only slightly over-predicted by the simulation below 670 nm. At higher wavelengths, however, the measured values never reach the simulated thermal radiation and the theoretical solution exceeds the measured values by about 30%.

At altitudes of 51 km and 45 km, the simulated continuum radiation is lower than the experimental values at low wavelengths but the over-prediction at high wavelengths remains. At present, the reasons for this disagreement are not yet clear.

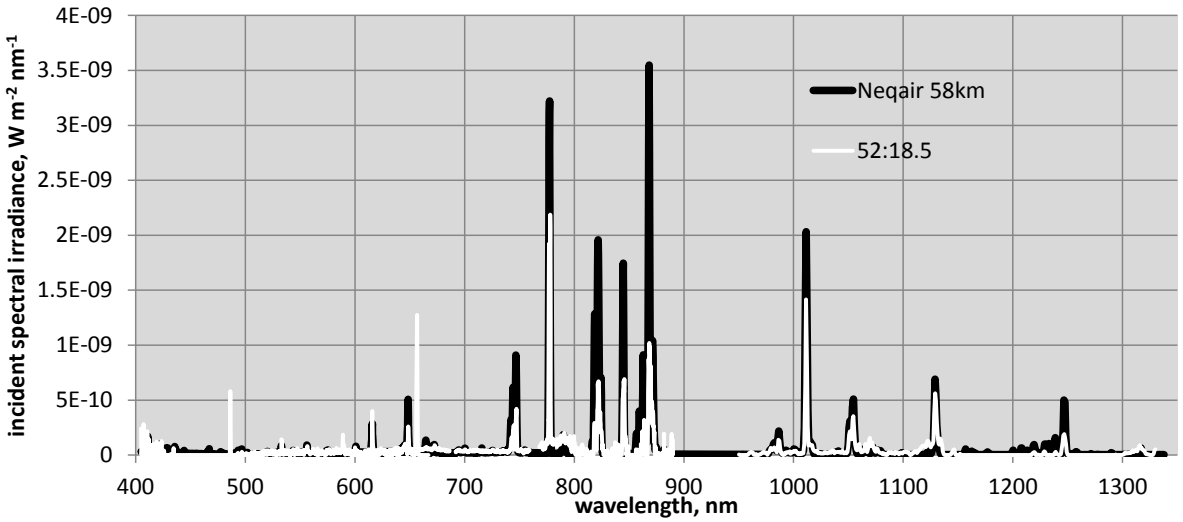

Fig. 24 Comparison of simulated atom line emission in the VIS to IR with combined spectra measured with the HDVS1, HDVS2, and IRIS instruments at 58km altitude.

To further investigate the plasma radiation, line spectra were isolated from the experimental spectra by subtracting a continuum radiation so that the signal around isolated lines would go to zero, and were compared to the *NEQAIR* simulation of the flow field before superposing the thermal radiation. Figure 24 shows an example of experimental and simulated spectra in the NIR around radiative peak heating at 58 km Hayabusa altitude. The spectra show fair agreement although the measured line intensities are in general lower than the simulation.

For a more detailed comparison, the line intensities of selected oxygen and nitrogen lines were integrated over the line width to compensate for possible discrepancies in simulated and experimental line width and shape. In Fig. 25, the resulting line integrals for strong oxygen lines at 777 nm and 845 nm, and nitrogen lines around 745 nm, 1013 nm, and 1250 nm are plotted vs. observation time. The general trend of the time variation is matched by the simulation but in the experiment, the atom lines disappear earlier than predicted, which can also be seen in the overview spectra at 51 km in Fig. 23. In early re-entry, the oxygen lines almost reach the predicted values but the simulated nitrogen lines are in general almost twice as strong as the measured ones.

These differences might partly be caused by the missing coupling between radiation and flow field which was not available for the numerical simulation conducted as the basis of simulated spectral emission. Studies for high speed re-entries [25,26,27] found uncertainties in radiative heating to the surface to be about ±30% for lunar return. Both radiation-flow field coupling and inclusion of ablation products were found to also change the shock stand-off distance. Future work should incorporate these two effects into the numerical simulation since it remains unclear how these values translate into uncertainties of, for example, one particular emission line.

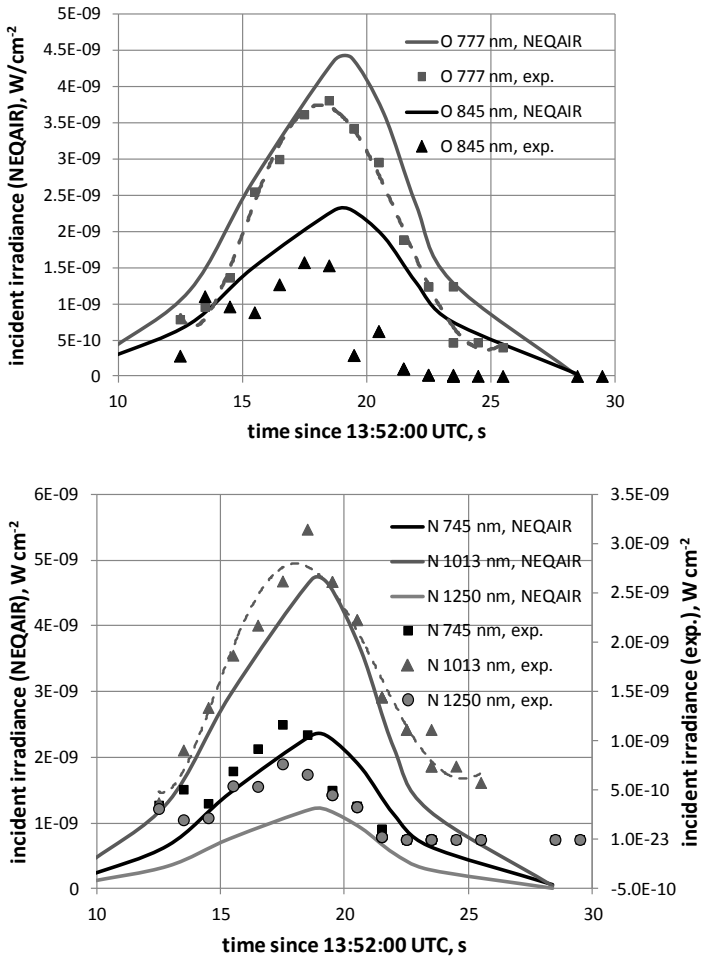

Fig. 25 Measured (IRIS data) and simulated line integrals for selected O and N lines vs. observation time. The dashed lines represent the trend of the experimental data for the strongest lines.

Finally, the spectroscopic data from the HDVS1 experiments and ground observation data were analyzed by fitting Planck radiation to the measured values at 548 nm yielding an experimentally derived effective averaged temperature [33]. The temperatures derived from the airborne observation data are in excellent agreement with those from the ground observation. If the same fitting procedure is applied to the simulation-based spectra, the corresponding simulated effective temperature is obtained, similar to the averaged temperatures already introduced in Fig. 18 but related to one wavelength (here 548 nm). The resulting temperatures from experiment and simulation are shown in Fig. 26 (a). Both shape and magnitude of these temperatures are in good agreement except for a shift in observation time. If the experimental data are shifted by -1.7 seconds (yielding a shift to higher Hayabusa altitudes), excellent agreement over the whole observed altitude range is achieved, as demonstrated in Fig. 26 (b). Since simulation and experimental data are linked through the observation time, a shift of +1.7 seconds within the

simulation (i.e., a delay of the entry interface) would have the same effect. However, no justification for such a shift in observation time can by justified from the reported uncertainties of the timing procedures for the experimental data or from the last known entry interface.

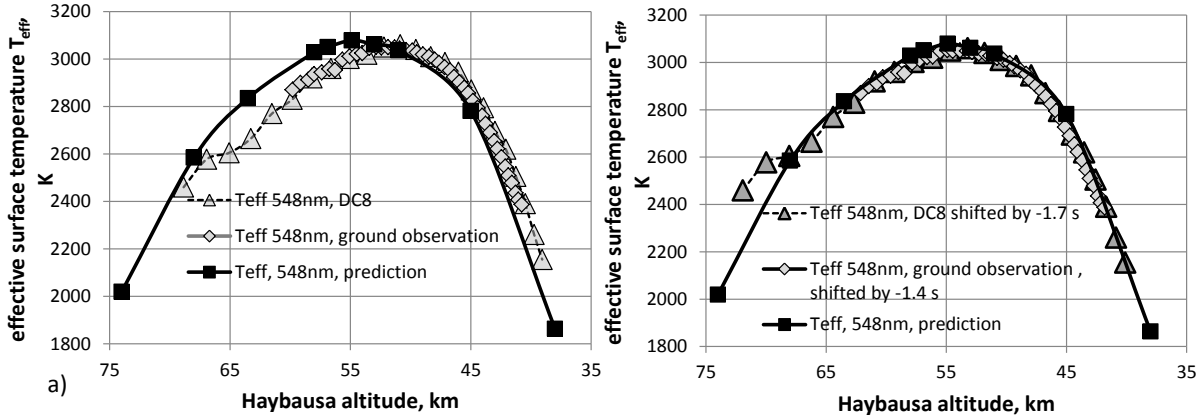

Fig. 26 Effective averaged surface temperatures for Planck radiation fitted at 548nm to the experimental HDVS1 data [33], to ground observation data [32], and to the simulated data for original timing (a) and for experimental data shifted by -1.7 and -1.4 seconds (b), respectively.

X. Conclusion and Summary

Using established practices for numerical simulation of flow and radiation fields, a baseline solution for the entry radiation signature of Hayabusa has been computed. A radiation prediction for the airborne observation of the Hayabusa reentry was performed on the basis of trajectory data and high fidelity CFD computations. Material response was taken into account to determine realistic surface temperatures of the capsule's heat shield to yield a prediction of the thermal radiation during reentry. The plasma radiation was computed with line by line methods. To enable a comparison of the predicted radiation with experimental data, the radiation had to be propagated from the Hayabusa position during reentry to the observer's position onboard the NASA DC-8.

A comparison with experimental data is encouraging and indicates that a first benchmark solution for the radiation prediction could be obtained with the present results. Emission spectra in the NIR with the NIRSPEC experiment show a good qualitative agreement but the prediction is clearly higher than the experimental data in that range. The comparison with UV spectra measured with the Australian AUS experiment shows excellent agreement with the thermal continuum portion of the simulated spectra. However, CN as the major radiator in that wavelength region is

not yet included in the CFD solution. The agreement of the experimental data with the thermal emission based on the current solution for laminar flow seems to confirm the assumption that no transition to turbulent flow occurred, as indicated by estimating a critical roughness Reynolds number from recession measurements and flow field data. A comparison with a larger data set provided by the Clay Center Observatory showed fair agreement of thermal radiation at lower wavelengths but a clear over-prediction of thermal radiation in the NIR. Effective averaged surface temperatures estimated by fitting Planck radiation to the measured spectra at 548 nm shows excellent agreement with both airborne and ground based data if a time shift of -1.7 seconds is applied to the experiment, basically assigning the experimental data to higher altitudes. This time shift seems consistent with the comparison of the spectral data. Furthermore, the disagreement at higher wavelengths seems to be an indicator for an unidentified wavelength-dependent attenuation. A spectral change in surface emissivity with lower values than assumed at wavelengths above 700 nm would bring the simulation closer to the experiment. However, it is questionable whether the required decrease to values around 0.7 could be justified. Oxygen atom line integrals were in fair agreement over a large part of the trajectory but all investigated nitrogen lines showed an over-prediction by a factor of two in the simulation. Independent of a possible unidentified attenuation, it can be seen that the atom lines fade out much earlier in the experimental data set than predicted by the simulation.

Given the high uncertainties related to the numerical simulation if current margin policies are used, an interpretation of the differences between simulation and experiments is considered premature. In fact, the purpose of these observation campaigns is to provide an experimental basis to determine these uncertainties from a comparison with simulation and improve the fidelity of models used in the predictions through sensitivity studies.

The procedure outlined here shows some differences from earlier approaches applied to the analysis of the observation of the Stardust reentry, in particular in handling thermal radiation. It appears highly desirable to revisit the Stardust radiation predictions and repeat both methodologies to quantify the differences. To further improve the predictions, an implementation of a blowing surface with ablation and pyrolysis products would be valuable, as these data sets will give a unique opportunity to test such models versus a real flight situation. In addition, radiation-flow field coupling might change the results of the numerical simulation and is highly recommended for future work. For future experimental investigations, additional onboard measurements with flight experiments at dedicated vehicle positions would strengthen the outcome substantially.

Acknowledgments

The observation campaign was funded and managed by the *Orion Thermal Protection System Advanced Development Project* and the *NASA Engineering and Safety Center*. The present work was supported by NASA Contract NAS2-03/44 to UARC, UC Santa Cruz, and by NASA Contract NNA10DE12C to ERC, Incorporated. The authors would like to thank George Raiche (Chief, Thermophysics Facilities Branch, NASA ARC) and Aga Goodsell (Chief, Aerothermodynamics Branch, NASA ARC) for support of modeling and simulation aspects of the present work. Furthermore, the authors wish to acknowledge the support of Jay Grinstead, NASA Ames, Alan Cassell, ERC, Inc., and Jim Albers, for mission planning and for providing trajectory information, and Nicholas Clinton and Jeffrey Myers, UARC, for compiling *MODTRAN* computations for atmospheric extinction as well as Jonathan Snively (Embry-Riddle Aeronautical University), Mike Taylor (Utah State University), David Buttsworth, Richard Morgan (University of Southern Queensland), Ronald Dantowitz, and Marek Kozubal (Clay Center Observatory) for providing experimental data for a comparison with the predictions, Dinesh Prabhu, ERC, Inc., for numerous discussions about all mission and simulation aspects, Mike Olsen, NASA Ames, for his help during the spectral computations, and Mike Wilder, NASA Ames, and Brett Cruden, ERC, Inc., for valuable comments during the review process.

References

[1] Jenniskens, P., Kozubal, M.J., Dantowitz R.F., Breitmeyer, J., Winter, M.W., Grinstead J.H.,, Loehle, S., "Time-resolved absolute irradiance of the Hayabusa Sample Return Capsule Reentry," 50th AIAA Aerospace Sciences Meeting including the New Horizons Forum and Aerospace Exposition, 9 - 12 Jan 2012, Nashville, Tennessee. https://doi.org/10.2514/6.2012-1294

[2] Watanabe, J., Ohkawa, T., Sato, M., Ohnishi, Iijima, Y., Kagaya, Y., Tanabe, T., "Expedition for a Ground-Based Observation of HAYABUSA Spacecraft Re-Entry," Publications of the Astronomical Society of Japan, Volume 63, Issue 5, 25 October 2011, Pages 941–946, https://doi.org/10.1093/pasj/63.5.941

[3] Wright, M. J., Candler, G. V., and Bose, D., "Data-Parallel Line Relaxation Method of the Navier-Stokes Equations," *AIAA Journal*, Vol. 36, No. 9, 1998, pp. 1603–1609. https://doi.org/10.2514/2.586

[4] Wright, M.W., White, T., and Mangini, N., "Data Parallel Line Relaxation (DPLR) Code User Manual Acadia – Version 4.01.1," NASA/TM-2009-215388, October 2009.

[5] Chen, Y.-K., and Milos, F.S., "Ablation and Thermal Analysis Program for Spacecraft Heatshield Analysis," *Journal of Spacecraft and Rockets*, Vol. 36, No. 3, 1999, pp. 475-483. https://doi.org/10.2514/2.3469

[6] Whiting, E. E., Park, C., Liu, Y., Arnold, J. O., and Paterson, J. A., NEQAIR96, "Nonequilibrium and Equilibrium Radiative Transport and Spectra Program: User's Manual, " NASA RP-1389, NASA, December 1996.

[7] Liu, Y., Prabhu, D., Trumble, K.A., Saunders, D., Jenniskens, P., "Radiation Modeling for the Reentry of the Stardust Sample Return Capsule," *Journal of Spacecrafts and Rockets*, Vol. 47, No. 5, September–October 2010. https://doi.org/10.2514/1.37813

[8] Winter, M.W., McDaniel, R.D., Chen, Y.-K., Liu, Y., Saunders, D., "Radiation Modeling for the Reentry of the Hayabusa Sample Return Capsule, " *International Planetary Probe Workshop IPPW8*, Portsmouth, Virginia, June 2011.

[9] Huo, W.M. "Electron-Impact Excitation and Ionization in Air, "AIAA 2008-1207, *46th AIAA Aerospace Sciences Meeting and Exhibit*, 7 - 10 January 2008, Reno, Nevada. https://doi.org/10.2514/6.2015-1896

[10] Allen, G. A., Jr., Wright, M. J., and Gage, P., "The Trajectory Program (Traj): Reference Manual and User's Guide," NASA TM -2005-212847, 2005.

[11] Cassell, A.M., Allen, G.A., Winter, M.W., Grinstead, J.H., Antimisaris, M.E., Albers, J, Jenniskens, P.M., "Hayabusa Reentry: Trajectory Analysis and Observation Mission Design," *42nd AIAA Thermophysics Conference*, 27 - 30 Jun 2011, Honolulu, Hawaii. https://doi.org/10.2514/6.2011-3330

[12] Queen, E. M., Cheatwood, F. M., Powell, R. W., Braun, R. D., and Edquist, C. T., "Mars Polar Lander Aerothermodynamic and Entry Dispersion Analysis," *Journal of Spacecraft and Rockets*, Vol. 36, No. 3, May-June 1999. https://doi.org/10.2514/2.3462

[13] Gnoffo, P. A., Weilmuenster, K. J., Braun, R. D., and Cruz, C. I., "Influence of Sonic-Line Location on Mars Pathfinder Probe Aerothermodynamics," *Journal of Spacecraft and Rockets*, Vol. 33, No. 2, March-April 1996. https://doi.org/10.2514/3.26737

[14] Yee, H. C., "A Class of High-Resolution Explicit and Implicit Shock Capturing Methods," NASA TM 101088, Feb. 1989.

[15] MacCormack, R. W. and Candler, G. V., "The Solution of the Navier-Stokes Equations Using Gauss-Seidel Line Relaxation," *Computers and Fluids*, Vol. 17, No. 1, 1989, pp. 135-150. https://doi.org/10.1016/0045-7930(89)90012-1

[16] Gupta, R., Yos, J., Thompson, R., and Lee, K., "A Review of Reaction Rates and Thermodynamic and Transport Properties for and 11-Species Air Model for Chemical and Thermal Nonequilibrium Calculations to 30,000 K," NASA RP-1232, Aug. 1990.

[17] Ramshaw, J. D., "Self-Consistent Effective Binary Diffusion in Multicomponent Gas Mixtures," *Journal of Non-Equilibrium Thermodynamics*, Vol. 15, No. 3, 1990, pp. 295-300. https://doi.org/10.1515/jnet.1990.15.3.295

[18] Park, C. *Nonequilibrium Hypersonic Aerothermodynamics*, Wiley, 1990, ISBN-13: 978-0471510932.

[19] Gordon, S., and McBride, B., "Computer Program for Calculation of Complex Chemical Equilibrium Compositions and Applications," NASA Ref. Publ. 1311, 1994.

[20] Yamada, T., Inatani, Y., Hirai, N.I.K., Morita, S., "Reentry of Hayabusa Sample Return Capsule and Post-Flight Analysis of the Recovered Heatshield," AIAA 2011-3322, *42nd AIAA Thermophysics Conference*, 27 - 30 June 2011, Honolulu, Hawaii. https://doi.org/10.2514/6.2011-3322

[21] Daniel Reda, Michael Wilder, Dinesh Prabhu, "Transition Experiments on Slightly Blunted Cones with Distributed Roughness in Hypersonic Flight," AIAA Journal, Vol. 50, No. 10 (2012), pp. 2248-2254. https://doi.org/10.2514/1.J051616

[22] *Gridgen*, Version 15.09, Pointwise, Inc., Forth Worth, TX.

[23] National Oceanic and Atmospheric Administration, National Aeronautics and Space Administration, U. S. Air Force, "U.S. Standard Atmosphere 1976," U. S. Government Printing Office, Washington, DC, 1976.

[24] Justus, C. G., and D. L. Johnson (1999), "The NASA/MSFC Global Reference Atmospheric Model - 1999 Version (GRAM-99)," NASA TM-1999-209630.

[25] Johnston, C., Kleb, B., "Uncertainty Analysis of Air Radiation for Lunar Return Shock Layers," Journal of Spacecraft and Rockets, Vol. 49, No. 3 (2012), pp. 425-434. https://doi.org/10.2514/1.A32161

[26] A. M. Brandis, A.M., Johnston, C. O., Cruden, B. A., Prabhu, D., Bose, D., "Uncertainty Analysis and Validation of Radiation Measurements for Earth Reentry," Journal of Thermophysics and Heat Transfer, April 2015, Vol. 29, No. 2 : pp. 209-221. https://doi.org/10.2514/1.

[27] Johnson, C.O., Brandis, A.M., Bose, D., "Radiative Heating Uncertainty for Hyperbolic Earth Entry, Part 3: Comparisons with Electric Arc Shock-Tube Measurements," Journal of Spacecraft and Rockets, January 2013, Vol. 50, No. 1 : pp. 48-55. https://doi.org/10.2514/1.A32484

[28] Anderson, G. P., A. Berk, P. K. Acharya, M. W. Matthew, L. S. Bernstein, J. H. Chetwynd, H. Dothe, S. M. Adler-Golden, A. J. Ratkowski, G. W. Felde, J. A. Gardner, M. L. Hoke, S. C. Richtsmeier, B. Pukall, J. Mello and L. S. Jeong, "MODTRAN4: Radiative Transfer Modeling for Remote Sensing," in *Algorithms for Multispectral, Hyperspectral, and Ultraspectral Imagery VI*, Sylvia S. Chen, Michael R. Descour, Editors, Proceedings of SPIE Vol. 4049, pg. 176-183, 2000. https://doi.org/10.1117/12.410338

[29] Palmer, G., "Uncertainty Analysis of CEV LEO and Lunar Return Entries," AIAA Paper No. 2007-4253, 9th AIAA Thermophysics Conference, Fluid Dynamics and Co-located Conferences, June 2007. https://doi.org/10.2514/6.2007-4253

[30] Wright, M.J., Bose, D., and Chen, Y.-K., "Probabilistic Modeling of Aerothermal and Thermal Protection Material Response Uncertainties for Aerocapture Using Rigid Aeroshells," AIAA Journal, Vol. 45, No. 2, 2007, pp. 399-410. https://doi.org/10.2514/1.26018

[31] Johnson H. L., "A photometric system," Annales d'Astrophysique 18, 292-316, 1955.

[32] Buttsworth, D., Morgan, R., Jenniskens, P., "Near-Ultraviolet Emission Spectroscopy of the Hayabusa Reentry", Journal of Spacecraft and Rockets, Vol. 50, No. 6 (2013), pp. 1109-1120. https://doi.org/10.2514/1.A32500.

[33] Buttsworth, D., Jacobs, P., Potter, D., Mudford, N., D'Souza, M., Eichmann, T., Morgan, R., Jenniskens, P., McIntyre, T., Jokic, M., Jacobs, C., Upcroft, B., Khan, R., Porat, H., and Neely, A., "Super-orbital Re-entry in Australia – laboratory measurement, simulation and flight observation," 28th International Symposium on Shock Waves, 17 - 22 July 2011, Manchester, UK.

[34] Snively, B. J., Taylor, M. J., Jenniskens, P. M., Winter, M. W., Kozubal, M., Dantowitz, R., Breitmeyer, J., "Near-Infrared Spectroscopy of Hayabusa Sample Return Capsule Reentry," ournal of Spacecraft and Rockets, March 2014, Vol. 51, No. 2 : pp. 424-429. https://doi.org/10.2514/1.A32520